Article

General theory for packing icosahedral shells into multi-component aggregates

Nicolò Canestrari, Diana Nelli ✉ & Riccardo Ferrando ✉

Multi-component aggregates are being intensively researched in various fields because of their highly tunable properties and wide applications. Due to the complex configurational space of these systems, research would greatly benefit from a general theoretical framework for the prediction of stable structures, which, however, is largely incomplete at present. Here we propose a general theory for the construction of multi-component icosahedral structures by assembling concentric shells of different chiral and achiral types, consisting of particles of different sizes. By mapping shell sequences into paths in the hexagonal lattice, we establish simple and general rules for designing a wide variety of magic icosahedral structures, and we evaluate the optimal size-mismatch between particles in the different shells. The predictions of our design strategy are confirmed by molecular dynamics simulations and density functional theory calculations for several multi-component atomic clusters and nanoparticles.

The research on multi-component nanoaggregates is very active and spans many different fields. High-entropy alloy nanocrystals, consisting of nanometre-sized solid solutions of five or more elements, have attracted much attention due to their enhanced structural stability and catalytic activity[1–4]. Ordered architectures are explored as well. Among them, the assembly of concentric shells of different compositions into multilayer aggregates is a widely employed tool to protect or functionalise the core[5,6], improve the stability[7–10], and adjust the surface properties[11,12] of the nanostructure.

The wide range of possible compositions and the huge configurational space of multi-component systems are key to their broad success. However, such inherent complexity poses major challenges to the design and synthesis of nanoaggregates with well-defined and durable configurations. A general theory for the prediction of stable multicomponent structures would be an essential reference for the design and synthesis of nanoparticles for customised applications. However, such a theory is lacking at present.

Here, we propose a theoretical approach which generalises and unify concepts from crystallography[13] and structural biology[14–16] to develop a design strategy of multi-component clusters and nanoparticles.

We consider multi-component aggregates formed by particles of different sizes and establish general criteria for assembling these particles into highly symmetric multi-shell structures. In particular, we apply our approach to icosahedral structures. Icosahedra combine the maximum symmetry with the most compact shape. These properties favour energy stability in clusters and nanoparticles[17,18] and give an evolutionary advantage in biological systems such as viruses[14,16,19]. Accordingly, icosahedra have been observed in a huge variety of systems, including clusters and nanoparticles[20–24], colloidal aggregates[25–27], intermetallic compounds and quasicrystals[28–30], viral capsids, bacterial organelles, DNA and protein aggregates[31–35].

Several research efforts can be found in the literature, starting with the seminal work of Caspar and Klug[14], dedicated to rationalising the structure of individual icosahedral shells, especially in the field of virus biology[15,16,36,37]. Icosahedral shells are made of one layer of particles, which can be arranged according to achiral or chiral symmetries. Chiral shells present all rotational symmetry operations of the icosahedron but lack its reflection planes.

On the contrary, there is no general theory for assembling together multiple shells of different radii, with achiral and chiral symmetries, into concentric arrangements to generate compact icosahedral aggregates. In metal nanoparticles and clusters, and in aggregates of colloidal particles, compact structures are much more commonly observed than single shells[17,20,21,24–27]. The theoretical efforts to assemble multi-shell icosahedra are rather limited. They began with

Dipartimento di Fisica, Università di Genova, Genova, Italy. ✉e-mail: diana.nelli@edu.unige.it; riccardo.ferrando@unige.it

the historical works of Bergman et al.[38] and Mackay[13], both concerning achiral structures only. In particular, Mackay constructed icosahedra by packing spheres of equal size arranged in shells around a central particle. Mackay icosahedra turns out to be built of 20 distorted tetrahedra, in which particle layers are arranged into the stacking of the face-centred cubic lattice (ABCABC...). Most icosahedra observed in metal clusters and nanoparticles are of Mackay type[20–22,24]. Mackay also proposed a possible termination by a single shell in hexagonal close-packed (hcp) stacking (giving, for example, the sequence ABCABCB), known as the anti-Mackay shell. Anti-Mackay terminations have been recently observed in colloidal aggregates[25,26]. Even fewer theoretical efforts have been devoted to constructing icosahedra that include chiral shells. These efforts have been limited to adding a single chiral shell on top of an achiral Mackay core[39–41].

The key point of our theoretical approach is the mapping of multi-shell structures into paths in the hexagonal lattice. The mapping naturally leads to the design of multi-shell sequences corresponding to an alternative series of icosahedral magic numbers. Furthermore, the mapping allows us to predict which sequences exhibit spontaneous symmetry breaking from achiral to chiral structures. In the field of metal clusters and nanoparticles, chiral icosahedra are especially interesting for their applications to catalysis[41]. In all cases, we demonstrate that icosahedra are stabilised by the size mismatch between particles of different shells and evaluate the optimal mismatch for energetic stability. We note that, due to the contraction of pair distances between particles in adjacent shells[13], the icosahedron is naturally suitable for accommodating particles of different sizes in different shells. Our approach is generalised also to anti-Mackay shells, so that it allows us to derive a design principle for the structures observed in colloidal aggregates[25–27], and to predict others.

Our design strategy is validated by numerical calculations for several model systems and by ab initio calculations for alkali metal clusters. The predictions of our theory are further confirmed by simulations of the growth of alkali and transition metal nanoparticles including up to four different elements. These simulations show that atoms naturally self-assemble into the predicted multi-shell icosahedral structures, including those with symmetry-breaking shell sequences. Although the applications presented below concern atomic clusters and nanoparticles, due to the general character of its basic assumptions, our theory can be applied to the design of aggregates of other particle types, such as aggregates of colloidal particles and complex molecules of biological interest.

Results

Mapping icosahedra into paths

Here, we develop our theoretical framework, whose starting point is the well-known approach of Caspar and Klug (CK)[14–16], which was originally proposed for rationalising and predicting the architecture of icosahedral viral capsids. Specifically, they developed a general method for the construction of individual icosahedral shells, which is based on cutting and folding leaflets from the two-dimensional hexagonal lattice and produces achiral and chiral arrangements of particles on the icosahedral surface.

The CK construction is shown in Fig. 1a. A segment is drawn between points of coordinates $(0, 0)$ and (h, k) with respect to the basis vectors of the hexagonal lattice; h and k are integer non-negative numbers so that the segment always connects two lattice points. The segment is the base of an equilateral triangle, which is replicated 20 times to form a leaflet, which is then cut and folded to generate an icosahedral shell with a well-defined surface lattice.

In the CK theory, the triangulation number T of an icosahedral shell is defined as the square length of the triangular edge, and is calculated as $T = h^2 + k^2 + hk$. The edge and radius of the shell are $\sqrt{T}$ and $\sin(2\pi/5)\sqrt{T}$, respectively. Assigning one particle to each lattice

point, the shell contains $10\,T + 2$ particles (see Supplementary Note 1.1).

Shells are achiral or chiral depending on the angle θ_{CK} between the h-axis and the segment of the CK construction. Achiral shells correspond to segments with $\theta_{CK} = 0°$, $30°$ and $60°$. Segments on a coordinate axis correspond to the achiral shells described by Mackay (MC) in his work on the packing of equal spheres[13]. Shells built on segments on the diagonal ($h = k$, $\theta_{CK} = 30°$) are here called of Bergman (BG) type since the smallest is the outer shell of the Bergman cluster[30,38]. All other shells are chiral, with enantiomers symmetrically placed with respect to the diagonal. We remark that, in the CK theory, an icosahedral shell is uniquely determined by the segment endpoint (h, k) in the hexagonal lattice; therefore, in the following, icosahedral shells will be denoted by their (h, k).

We begin our generalised construction by grouping icosahedral shells into chirality classes. In Fig. 1b, points in the hexagonal lattice are coloured according to the chirality class of the corresponding icosahedral shell. From each lattice point on the diagonal, a chirality class originates, which we call Chn; this comprises the (n, n) BG shell, the shells with $h = n$ and $k > n$, and their enantiomers ($h > n$, $k = n$). For example, shells of the Ch1 class have either $h = 1$ or $k = 1$, whereas the second index increases starting from 1. MC shells are grouped into class Ch0, together with the one-particle shell $(0, 0)$. The radius and the number of particles in the shell increase with the non-constant index, so that larger and larger shells are found while moving farther from the diagonal. Shells within the same chirality class share a similar particle arrangement on the icosahedral surface, whereas shells belonging to different classes are clearly different (see Fig. 1c, d). The grouping of icosahedral shells into chirality classes is key to rationalise and predicting their optimal packing and their dynamic assembling into tightly packed structures. This will be clarified and deeply discussed in the following.

The main point of our construction consists of assembling concentric shells into aggregates by drawing paths in the hexagonal lattice. As a first example, we consider a path along a coordinate axis, e.g., the k axis (Fig. 2a), starting from $k = 0$ and making steps $(0, k) \rightarrow (0, k+1)$ up to $k = i - 1$. This path assembles i concentric MC shells of larger and larger size into a Mackay icosahedron[13,17], a well-known structure observed in many experiments on clusters[20,21,24,42,43], which is thus recovered as a special case of our construction. Mackay icosahedra are tightly packed structures consisting of 20 distorted tetrahedra[17] in which the particles are arranged according to the face-centred-cubic (fcc) lattice. The number of particles in an MC icosahedron made of i shells is $N_i = (10i^3 - 15i^2 + 11i - 3)/3$, which gives the series of magic numbers 1, 13, 55, 147, 309,...

In general, paths can be drawn by allowing different increments at each step. Here we deal with the simplest generalisation, which consists of choosing between $(h, k) \rightarrow (h, k+1)$ and $(h, k) \rightarrow (h+1, k)$ (other types of steps in the hexagonal plane will be discussed in the following). In this case, the number of shells in a path from the origin to a point (h, k) is $i = h + k + 1$. Such paths are inspired by the Mackay path of Fig. 2a, in which one index is incremented at steps of one, whereas the other is kept constant and equal to zero. Allowing for different elementary steps in the hexagonal plane allows the building of a wide variety of icosahedral structures, which retain the densely packed character of the Mackay icosahedron.

We distinguish three cases, as shown in Fig. 2b. If (h, k) is above the diagonal, the elementary move $(h, k) \rightarrow (h, k+1)$ conserves the chirality class of the shell, i.e., the shell we are adding belongs to the same class of the previous one. On the contrary, by the move $(h, k) \rightarrow (h+1, k)$ the chirality class is incremented. If (h, k) is below the diagonal, the opposite applies. For (h, k) in the diagonal, i.e., for shells of BG type, both steps conserve the class; specifically, the two steps are equivalent since the corresponding added shells are enantiomers, with the same size and particle arrangement but opposite chirality.
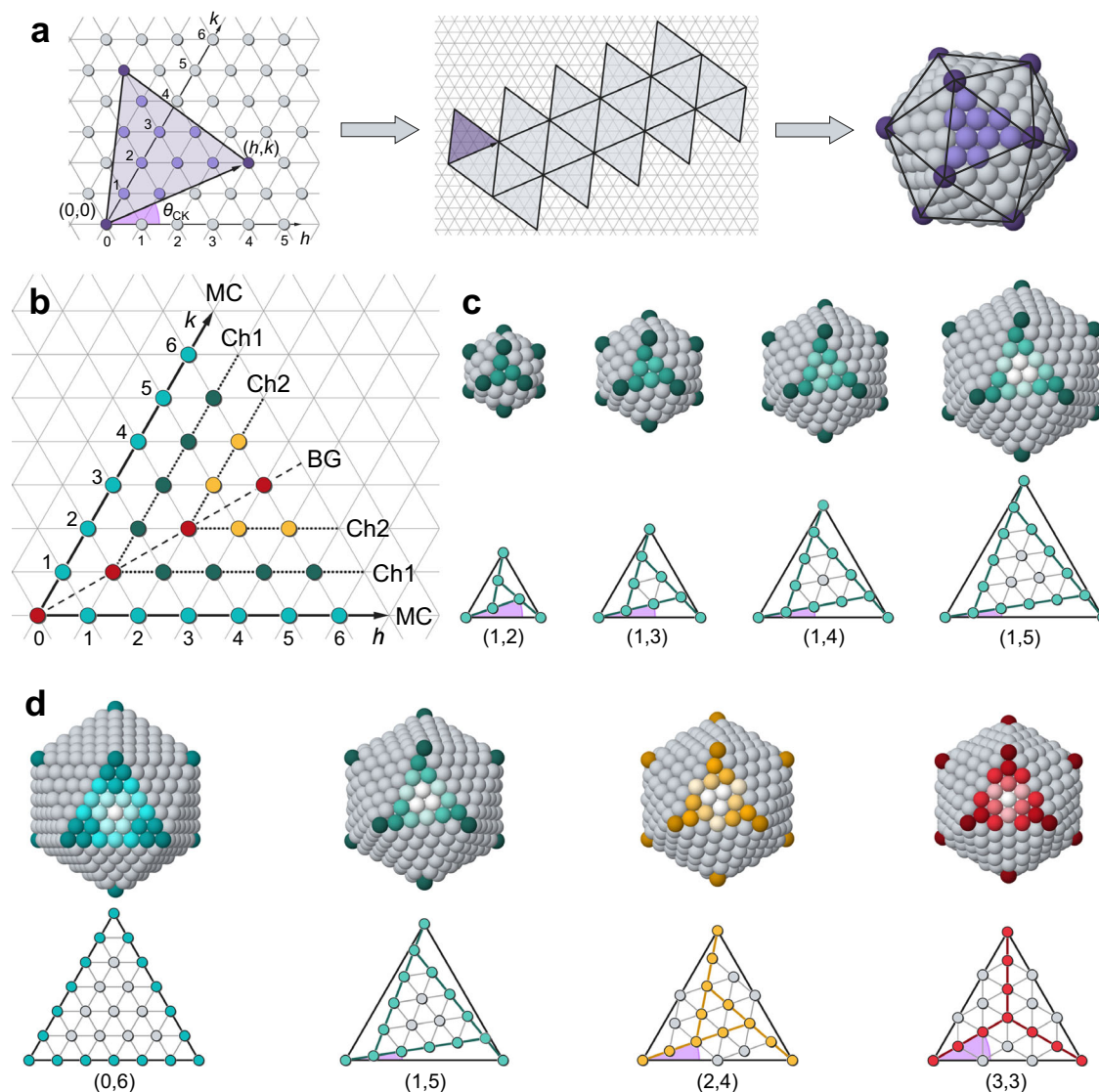
Fig. 1 | Caspar-Klug shells and chirality classes. a Caspar-Klug construction[14–16]. The coordinate axes h and k ((h, k) non-negative integers) are at 60°. From left to right: a segment from $(0, 0)$ to (h, k) is drawn and an equilateral triangle is constructed on it; the triangle is repeated 20 times to form a leaflet that is cut and folded into an icosahedral shell. **b** Correspondence between (h, k) points and icosahedral shells. The points on the coordinate axis (light blue) correspond to achiral MC shells[13,18], those on the diagonal (red) to achiral BG shells[30,38]. All other points correspond to chiral shells. Shells are grouped into classes Chn as explained in the text (MC ≡ Ch0). Green and red points correspond to Ch1 and Ch2 shells, respectively. **c** The first four right-handed shells of the Ch1 class. The triangles in the bottom row (identified by their (h, k)) show the angle $\theta = 60° - \theta_{CK}$ between the facet edge and the line connecting the vertex to a nearest neighbour point, that decreases with increasing k. **d** Achiral and right-handed shells with $h + k = 6$. From left to right, MC, Ch1, Ch2 and BG shells. θ increases from 0° to 30° from MC to BG. In the top rows of (**c** and **d**) the colour shades identify symmetrically equivalent particles.
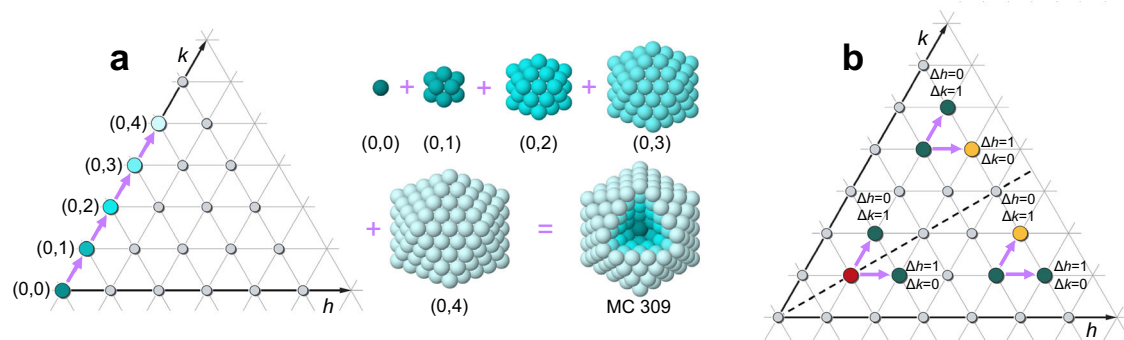

Fig. 2 | Mapping icosahedra into paths. a Path of a Mackay icosahedron: $i = 5$ shells are assembled on top of each other. **b** The three possible cases when choosing between $(h, k) \rightarrow (h, k + 1)$ and $(h, k) \rightarrow (h + 1, k)$ at each step of the path. In (**b**) points are coloured according to the chirality class of the corresponding shell, as in Fig. 1b.

When assembling shells in physical systems, one must bear in mind that in the icosahedron, the radius is shorter than the edge by $\sin(2\pi/5) \approx 0.9511$, which has a direct effect on the packing of concentric shells. In the Mackay icosahedron of equal spheres[13], the distance between spheres in neighbouring shells is shorter by about 5% than that between spheres in the same shell. Similar considerations hold for shells belonging to other chirality classes, assembled according to the path rules identified so far; in some cases, the difference between intra-shell and inter-shell nearest-neighbour distances is even larger. These considerations naturally lead to the idea of assembling shells in which particles in different shells have different sizes, which we better clarify below.

We consider the case of a core with i shells, to which we add the outer shell $i + 1$. Particles in the core and in the outer shell have different sizes. We define the size mismatch $sm_{i,i+1} = (d_{i+1} - d_i)/d_i$, with d_{i+1} and d_i particle sizes in shells $i + 1$ and i, respectively.

In the example of Fig. 3a, b, the core is made of five MC shells, i.e., it is terminated by the (0, 4) shell. According to our path rules, the outer shell can be either the (0, 5) MC shell (same class) or the (1, 4) Ch1 shell (different class). We consider a simple model, in which all particles interact by the well-known Lennard-Jones (LJ) potential; specifically, the interaction energy is the same for all particles, the only difference being the equilibrium distance of pair interactions, which accounts for particles of different sizes (see the Methods section). In Fig. 2a, we calculate the binding energy depending on the size mismatch and determine the mismatch that minimises the energy of the whole aggregate. For both MC and Ch1 shells, this optimal mismatch is

positive, i.e., it is favourable to have bigger particles in the outer shell than in the core, and it is larger for Ch1 than for MC shells.

The optimal mismatch can be estimated also by geometric packing arguments, which are discussed in detail in Supplementary Note 1. Here we recall only the main assumption and give the final result. In order to evaluate the optimal mismatch between particles of shells i and $i + 1$ it is reasonable to impose that

$$r_{i+1} - r_i = \frac{d_i + d_{i+1}}{2} \tag{1}$$

where r_i and r_{i+1} are the radii of the respective shells, d_i and d_{i+1} are the particle diameters in these shells. For atomic systems, these diameters are estimated from the nearest-neighbour distance of atoms in their crystal lattice. Recalling that the relation between the radii and the triangulation numbers of the shells

$$r_i = d_i \sin\left(\frac{2\pi}{5}\right)\sqrt{T_i} \tag{2}$$

one finally obtains the following approximate expression for the optimal size mismatch

$$sm_{i,i+1} = \frac{2\sin\left(\frac{2\pi}{5}\right)(1+\xi)\sqrt{T_i}+1}{2\sin\left(\frac{2\pi}{5}\right)\sqrt{T_{i+1}}-1} - 1. \tag{3}$$
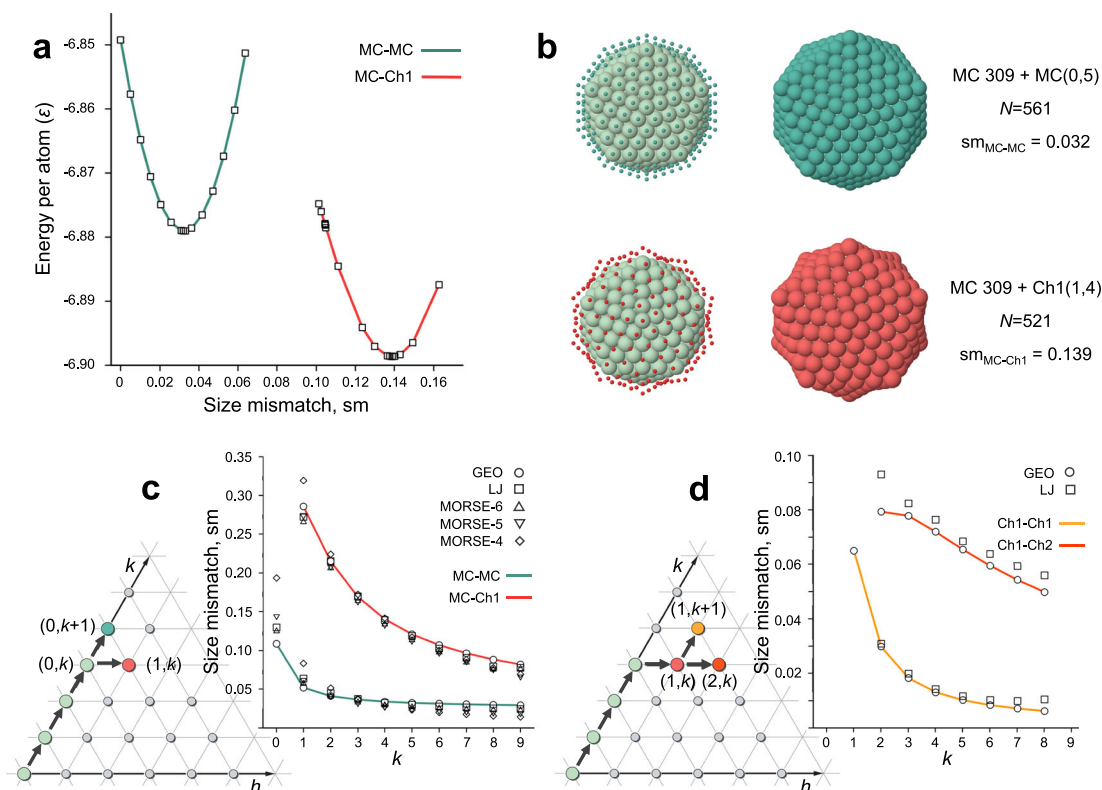

Fig. 3 | Optimal size mismatch. a Binding energy per atom for clusters made of a core with five MC shells plus a sixth shell, which is either MC (blue curve) or Ch1 (red curve). Interactions are of Lennard-Jones (LJ) type (see "Methods"). The particles of the sixth shell differ from those in the core only by their size. The energy is in units of the ε of the LJ potential. The structures are shown in (**b**). **c** Comparison of the optimal mismatch between steps $(0, k) \to (0, k + 1)$ (blue curve) and $(0, k) \to (1, k)$ (red curve), corresponding to additional MC and Ch1 shells on an MC core, respectively. The optimal mismatch of Eq. (3) (GEO values) is compared to LJ and Morse potential

results. The Morse potential data are given for three values (4,5,6) of the parameter α, that regulates the width of the potential well (see the Methods section). **d** Comparison between steps $(1, k) \to (1, k + 1)$ (yellow curve) and $(1, k) \to (2, k)$ (orange curve), corresponding to additional Ch1 and Ch2 shells on a core containing k MC and one Ch1 shells, respectively. The optimal mismatch of Eq. (3) (GEO) is compared to LJ data. Source data of (**a**, **c**, **d**) are provided as a Source Data file.

Here, $\xi \ll 1$ is an expansion coefficient of pair distances in the core, which depends on the number and the type of shells of the same component in the core (see Supplementary Note 1.4).

In Fig. 3c, d the results of Eq. (3) are compared to those for LJ and Morse clusters. Data in Fig. 3c are obtained as in Fig. 3a, but for different sizes of the Mackay core, whereas in Fig. 3d we consider a cluster made of a Mackay core plus a Ch1 shell, to which we add a further shell of either Ch1 or Ch2 type. In all cases the agreement is good. Eq. (3) is thus a reliable guide for the semi-quantitative evaluation of the optimal mismatch, which demonstrates the key role of geometric factors in determining it.

For the paths of Fig. 3, the optimal mismatch is always positive, i.e., icosahedral aggregates benefit from having bigger particles in the outer shells; in addition, much larger mismatches are found for class-changing than for class-conserving steps. These features are general for all icosahedra constructed according to the path rules identified so far, and are key to design stable icosahedral aggregates and to predict their natural growth modes.

Design strategy for icosahedral aggregates
Our theory is now applied to the path-based design of icosahedral aggregates. In order to construct a multi-shell icosahedral aggregate, a path is drawn according to the rules in Fig. 2 and, for each step, the optimal mismatch is estimated by Eq. (3). Then, particles of the appropriate sizes are associated with each shell.

An example is shown in Fig. 4, where the path connecting BG shells through neighbouring chiral shells is considered (Fig. 4a). This path alternates class-conserving and class-changing steps, spontaneously breaking mirror symmetries after the first BG shell. It produces a series of magic numbers

$$N_i = \frac{1}{4}(10\,i^3 - 15\,i^2 + 18\,i - b),\qquad(4)$$

with $b = 4$ and $b = 9$ for even and odd i, i.e., $N_i = 1, 13, 45, 117, 239, 431, \ldots$ (see Supplementary Note 1.2).

The path of Fig. 4a is used to design multi-species alkali clusters. The values of size mismatch between alkali atoms, estimated from nearest-neighbour distances in bulk crystals, are in the range of the optimal values for this path (Fig. 4b). In addition, these species present a weak tendency to mix and the bigger atoms have smaller cohesive energy; this produces a general tendency for the bigger atoms to stay in the surface layers, which, as we have seen in the previous section, is exactly what is needed for stabilising icosahedral aggregates.

The clusters in Fig. 4c correspond to $i = 3$ ($Na_{13}@K_{32}$, $Na_{13}@Rb_{32}$) and to $i = 4$ ($Na_{13}@K_{32}@K_{72}$, $Na_{13}@Rb_{32}@Rb_{72}$, $Na_{13}@K_{32}@Rb_{72}$). In these clusters, the atomic species is always changed in class-changing

steps, where a large mismatch is required, while it is changed or not in class-conserving steps, where the optimal mismatch is moderate, and therefore zero mismatch is expected to be acceptable.

The energetic stability of these clusters is verified in two ways: by full global optimisation searches using a semi-empirical force field, and by density functional theory (DFT) calculations on atomic pair exchanges (see Methods for details). Our global optimisation searches find that the structures designed according to the path in Fig. 4 are the lowest in energy for various binary and ternary alkali systems. Complete discussion and data are reported in Supplementary Note 4.1. The DFT data are reported in Figure 5 and Supplementary Tables 1–3 of Supplementary Note 2. In the case of CK shell sequences, exchanges of pairs of different atoms in adjacent shells produce energy increases. In contrast, if MC shells of these species are assembled in the same order, the resulting clusters are energetically unstable with respect to exchanges of atomic pairs, because the mismatch between species is too large for MC shells.

We have also checked the thermodynamic stability of MC@BG and MC@BG@Ch1 structures of Fig. 4c, by performing molecular dynamics simulations in which the temperature is progressively increased up to melting. Our simulations reveal that the global minimum structures are highly stable, as they do not undergo any structural transformation until the cluster entirely melts (see Supplementary Note 4.2).

Our theory, therefore, provides the possibility of constructing icosahedra in systems where the traditional Mackay icosahedra would not be stable.

Natural growth sequences
We have demonstrated how to geometrically construct multi-shell icosahedra and verified their energetic stability in various systems. Another important point is to understand how they grow dynamically in physical processes. To this end, we have performed molecular dynamics (MD) growth simulations[44], in which atoms are deposited on pre-formed clusters. This type of simulation has been used to interpret previous nanoparticle growth experiments[24,44]. The results are shown in Fig. 6 and in Supplementary Figs. 7–11 of Supplementary Note 3.1.

As a first case, we consider the growth of multi-element alkali clusters. In the previous section we have demonstrated the stability of non-trivial multi-shell structures, which comprise BG and chiral shells in the same aggregate. Here, we check whether these structures can be grown in a physically realistic process. Here, and in the following, growth temperatures are chosen to be significantly lower than the melting temperatures of the clusters.

When starting from a $Na_{13}@Rb_{32}$ cluster (Fig. 6a), consisting of shells (0, 0), (0, 1) and (1, 1), our rules of Fig. 2b predict that the next shell should be of Ch1 type, i.e., (1, 2) (or equivalently (2, 1)), regardless
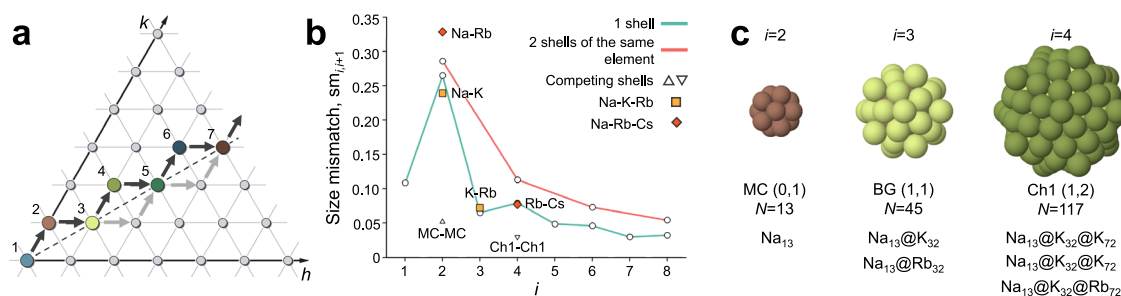

Fig. 4 | A path with spontaneous symmetry breaking. a A path connecting all BG shells through their nearby chiral shells. Black and grey arrows indicate paths with right and left-handed chiral shells. A generic path of this type may alternate both chiralities, corresponding to combinations of black and grey arrows. Shells are enumerated along the black-arrow path. b Optimal mismatch $sm_{i,i+1}$ according to Eq. (3) for the path in (a). Points connected by blue and red lines correspond to

changes of species in every shell and every two shells. The optimal values of $sm_{i,i+1}$ are compared to the mismatch between pairs of atomic species, indicated by squares and diamonds. The triangles correspond to the optimal mismatch between two MC shells and two Ch1 shells. c Structures for $i = 2, 3, 4$ along the path of (a), with their compositions related to specific systems. Source data of (b) are provided as a Source Data file.
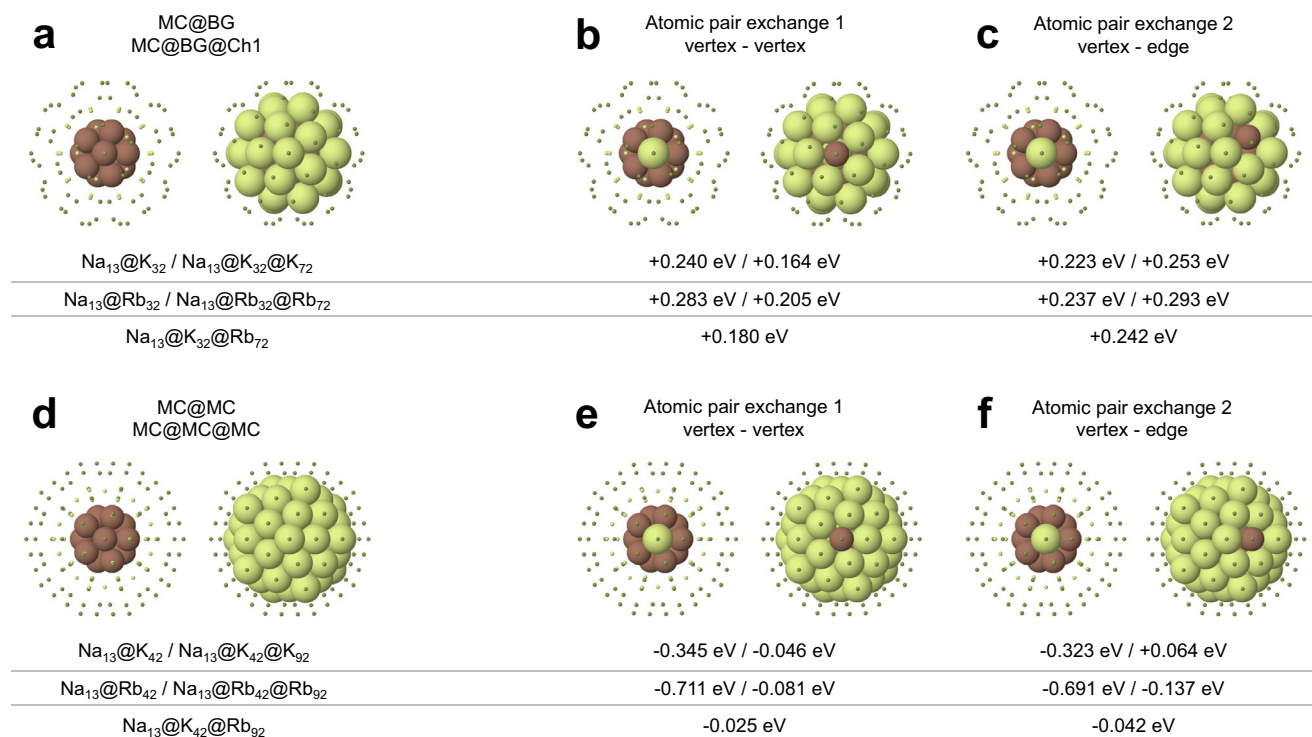
	a MC@BG MC@BG@Ch1	**b** Atomic pair exchange 1 vertex - vertex	**c** Atomic pair exchange 2 vertex - edge
	$Na_{13}@K_{32}$ / $Na_{13}@K_{32}@K_{72}$	+0.240 eV / +0.164 eV	+0.223 eV / +0.253 eV
	$Na_{13}@Rb_{32}$ / $Na_{13}@Rb_{32}@Rb_{72}$	+0.283 eV / +0.205 eV	+0.237 eV / +0.293 eV
	$Na_{13}@K_{32}@Rb_{72}$	+0.180 eV	+0.242 eV

	d MC@MC MC@MC@MC	**e** Atomic pair exchange 1 vertex - vertex	**f** Atomic pair exchange 2 vertex - edge
	$Na_{13}@K_{42}$ / $Na_{13}@K_{42}@K_{92}$	-0.345 eV / -0.046 eV	-0.323 eV / +0.064 eV
	$Na_{13}@Rb_{42}$ / $Na_{13}@Rb_{42}@Rb_{92}$	-0.711 eV / -0.081 eV	-0.691 eV / -0.137 eV
	$Na_{13}@K_{42}@Rb_{92}$	-0.025 eV	-0.042 eV

Fig. 5 | DFT data for atomic pair exchanges. Perfect structures before the atomic pair exchange, either of (**a**) MC@BG/MC@BG@Ch1 or (**d**) MC@MC/MC@MC@MC type. Atoms in the second and third shells are coloured in brown and yellow, respectively. **b**, **c**, **e**, **f** configurations after the atomic pair exchanges of two different types. Energy differences with respect to the perfect configurations in (**a**) and (**d**) are reported below. Positive and negative energy differences indicate unfavourable and favourable exchange processes, respectively. Complete data are reported in Supplementary Tables 1–3.

of the size mismatch. Therefore, even when depositing atoms of the same type, we expect such symmetry breaking to take place. This is indeed the case, as shown in Fig. 6a, in which in the first step of the growth a (1, 2) shell spontaneously form, leading to the $Na_{13}@Rb_{32}@Rb_{72}$ cluster. The symmetry breaking upon deposition of the same species of atoms is specific to BG shells. In contrast, the growth on the other type of achiral shell, i.e., MC shell, continues without symmetry breaking if atoms of the same species are deposited[24].

At this point, according to our rules, two non-equivalent steps are possible: the class-conserving step to (1, 3) and the class-changing step to (2, 2). These steps correspond to different optimal mismatches, i.e., 0.06 and 0.11, respectively, as estimated by Eq. (3). Since we are keeping on depositing Rb atoms (i.e., with zero mismatches), we expect growth to proceed by the (1, 3) step, which has the lower optimal mismatch. Again, our prediction is verified by the growth simulation of Fig. 6a, which further continues within the Ch1 class.

To change class after the shell (1, 2), it is necessary to deposit atoms of a bigger size than Rb. Specifically, the mismatch should be large enough to make the formation of the Ch1 (1, 3) shell unfavourable, thus addressing the growth towards the Ch2 class. At least, the mismatch between Rb and the deposited species should be larger than 0.06, which is the optimal value for the formation of the Ch1 shell. From Fig. 4b, it appears that Cs atoms have the right size (the mismatch between Rb and Cs is 0.08) and in fact, depositing Cs atoms on $Na_{13}@Rb_{32}@Rb_{72}$ (Fig. 6b) results in a transition to the Ch2 class, as shells (2, 2) and then (2, 3) form spontaneously during the growth.

Further confirmation of path rule predictivity is provided in Fig. 6c–e. In Fig. 6c, the size mismatch for the pairs AuNi, AuCo, AuFe, AgNi, AgCo, and AgCu is compared with the optimal estimates obtained from Eq. (3) for the addition of one MC and one Ch1 shell on a Mackay core. The mismatch much better corresponds to Ch1 than to

MC shells. For AuCo, AuFe, AuNi, AgNi and AgCo, Ch1 shells should grow on Mackay cores of 147 or 309 atoms (k = 3 or 4), while for AgCu the core should be larger, of 561 atoms (k = 5). This is confirmed by MD simulations (Fig. 6d–e) in which a Ch1 shell spontaneously forms when depositing Ag atoms on Ni_{147} or Cu_{561} Mackay cores. The growth continues within the Ch1 class if further Ag atoms are deposited. More results are presented and discussed in Supplementary Note 3.

We have verified that these structures are energetically stable. Icosahedra made of a Ni, Cu or Co Mackay core surrounded by one Ch1 shell of Ag atoms are the lowest in energy in several cases[39]. When adding a second Ch1 shell, the structures are not the lowest in energy any more, but they are in close competition with the global minima (see Supplementary Note 4.1). Anyway, when heated up by molecular dynamics simulations, these MC@Ch1@Ch1 clusters preserve their structure up to the melting temperature. Data are reported in Supplementary Note 4.2.

In summary, the growth on top of icosahedral seeds naturally proceeds according to our rules for drawing paths in the hexagonal plane. At each stage of the growth, two possible steps (class-changing or class-conserving step) are possible; among them, the system spontaneously takes the step that better fits the size mismatch between atoms of the pre-existing shell and those of the growing one. If atoms of the same species are deposited, i.e., with zero mismatches, the step associated with the lower optimal mismatch is taken, which is always the class-conserving step. If one continues to deposit atoms of the same type, further and further shells belonging to the same chirality class are formed. On the other hand, the class-changing step always requires the deposition of atoms of a different species with a larger radius and with a size mismatch close enough to the optimal one.

We note that almost perfect shell-by-shell growth is achieved in all simulations due to the fast diffusion of deposited atoms on top of the close-packed shells[24].
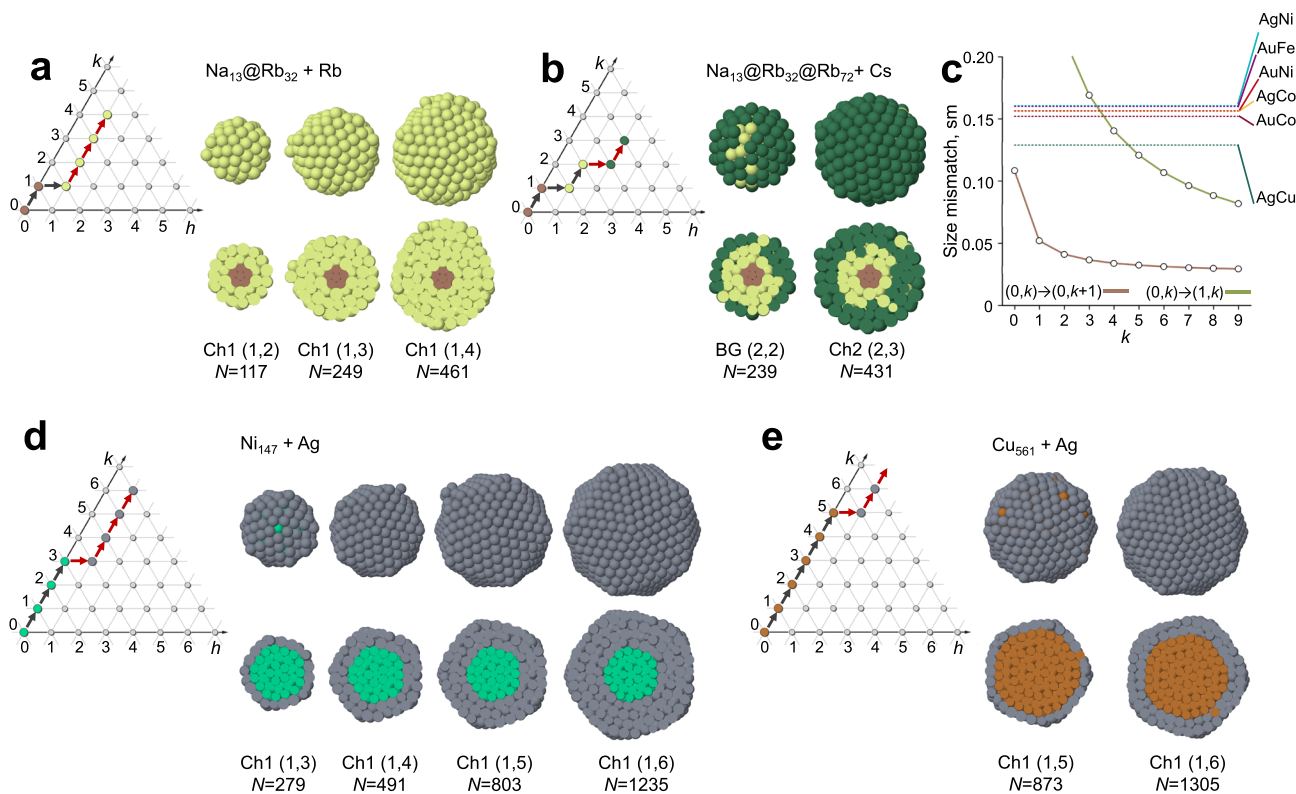
Fig. 6 | Growth sequences of chiral icosahedra. a Rb atoms are deposited on an icosahedral $Na_{13}@Rb_{32}$ seed. **b** The seed is $Na_{13}@Rb_{32}@Rb_{72}$, on which Cs atoms are deposited. **c** Size mismatch for some transition metal pairs compared to the optimal mismatch for a MC and a Ch1 shell on a MC core (brown and green lines, respectively), as a function of core size. **d**, **e** Snapshots from growth simulations and corresponding paths for the deposition of Ag atoms on (**d**) Ni_{147} and (**g**) Cu_{561} cores. All simulation snapshots in (**a**, **b**, **d**, **e**) are taken at magic sizes for the corresponding paths. In the top and bottom rows of the snapshot sequences, we show the cluster surface and its cross-section, respectively. In the representation of shell sequences in the hexagonal plane, black arrows are used to connect the shells belonging to the initial icosahedral seed, while red arrows connect the shells spontaneously formed on top of it in the growth simulations. Na, Rb, Cs, Ni, Cu and Ag atoms are coloured in brown, yellow, dark green, light green, orange and grey, respectively. Source data of (**c**) are provided as a Source Data file.

Here, we have shown and discussed the growth at some selected simulation temperatures. In Supplementary Note 3.4 we discuss the effect of temperature on the growth, showing that this type of icosahedral growth process is very robust, as it takes place in a wide range of temperatures.

Extension to anti-Mackay shells

The mapping of icosahedral structures into paths can be extended to other cases. Here, we establish the extension to the generalised anti-Mackay (AM) icosahedral shells of Fig. 7. AM shells are achiral and not close-packed, since they contain non-vertex particles with coordination lower than six. Each AM shell is identified by a pair of non-negative integers, which here we call (p, q), determining the disposition of particles in the triangular facet of the shell (see Fig. 7a). Shells with $q = 0$ have been described in the original work of Mackay[13], who proposed the possibility of adding to the fcc tetrahedra of the Mackay icosahedron one more shell in hexagonal close-packed (hcp) stacking. Multi-shell icosahedra terminated by AM shells of different types have been observed in confined aggregates of colloidal particles[25,27,45].

In Supplementary Note 1.5, we demonstrate that there is a correspondence between AM and CK shells (of chiral and BG type), as an AM shell of indexes (p, q) has the same number of particles of the CK shells with $h = q + 1$, $k = p + q$, if $k > h$, and $k = q + 1$, $h = p + q$ if $h > k$ ($p = 1$ gives the BG shells, that are common to AM and CK structures). Therefore, we can unambiguously identify an AM shell by the (h, k) indexes of a corresponding CK shell, and assign to it the same lattice point on the hexagonal plane. We group AM shells into AMn classes and denote an AM shell by $(h, k)^*$. The correspondence between AMn and Chn shells is explicitly shown in Fig. 7b, c for $n = 1, 2$.

AM shells can be packed by using the same rules described for CK ones. The same elementary steps in the hexagonal plane are allowed, but now one can decide whether to consider the CK or the AM shell corresponding to the endpoint of the step. In this way, a larger variety of icosahedra can be built. Again, the stability of these structures is ruled by the size mismatch between particles in different shells. The optimal size mismatch for icosahedra with AM shells can be estimated by using the same type of geometric considerations made for CK shells (see Supplementary Note 1.5).

In Fig. 8a we compare the stability of all possible shells that can be put on top of a Mackay core, namely MC, Ch1 and AM1. The optimal mismatch of the AM1 shells is intermediate between those of the MC and Ch1 shells (see also Supplementary Fig. 3). The mismatch for adding an AM1 shell on a 147-atom Mackay core is close to the one of AgCu so that an AM shell should grow by depositing Ag atoms on Cu a Mackay core of this size. This is verified by the MD simulations of Fig. 8b, in which we observe the formation of an Ag $(1, 3)^*$ shell.

From there on, the growth proceeds in a different way from that of Fig. 6e: a second shell of AM2 type is formed, followed by a shell of BG type, i.e., the class is changed at each step, even though atoms of the same type are deposited. This behaviour is due to the kinetic of the growth process. Specifically, it is due to fourfold adsorption sites on the surface of AM shells, which act as adatom traps and naturally lead to the formation of AM shells of higher class. The fourfold traps hinder the atomic mobility, causing a much rougher growth than in the case of Fig. 6e. This point is discussed in detail in Supplementary Note 3.3. We note that, even though kinetic effects dominate the process, the growth proceeds step by step by incrementing only one shell index, as predicted by our rules.
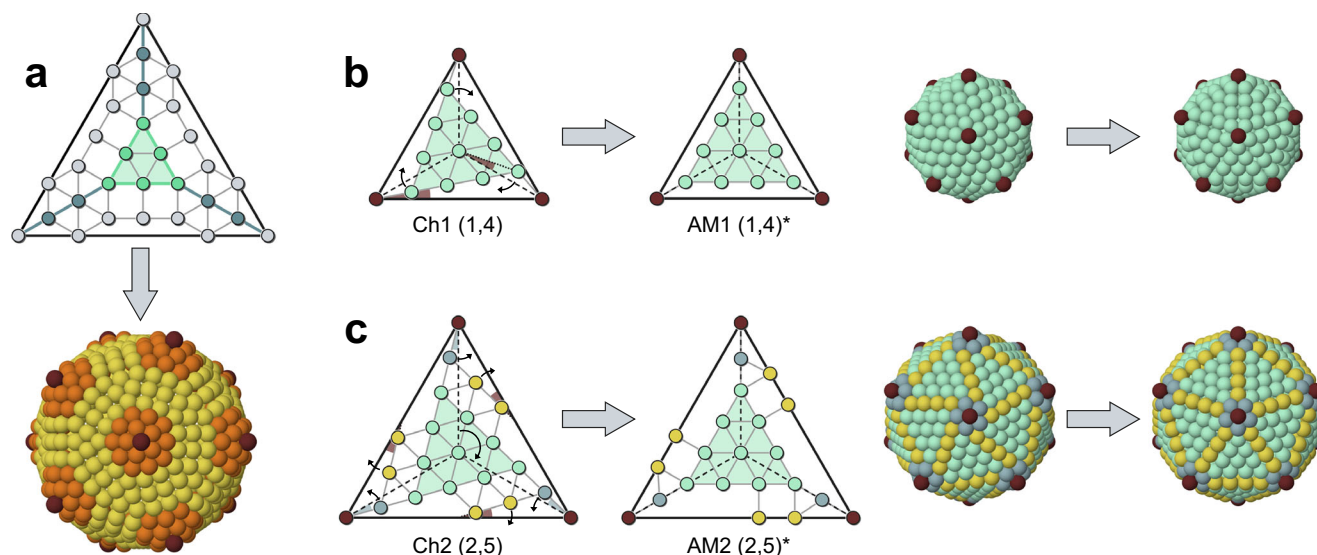
Fig. 7 | Generalised anti-Mackay shells. a A shell of the AM family. A facet and the complete shell are shown in the upper and lower panels. The shell is identified by (p, q), with p number of particles on the side of the inner triangle (light green particles in the top panel) and q number of particles between nearby vertices of the outer and inner triangles (blue particles). In this case, $(p, q) = (3, 2)$. In the bottom panel, orange particles have coordination 6 within the shell, while other particles have lower coordination. **b** AM1 ↔ Ch1 and (**c**) AM2 ↔ Ch2 correspondences. AM1 ↔ Ch1 amounts to the rotation of the inner triangles[39], whereas AM2 ↔ Ch2 involves rotations of different groups of particles, represented by different colours. A more detailed description is in Supplementary Note 1.5.

Finally, in Fig. 8c we show the growth of a ternary NiPdAg cluster. We start by depositing Pd atoms on a Ni_{147} Mackay cluster that spontaneously arranges into an anti-Mackay $(1, 3)^*$ shell. The mismatch between Ni and Pd is of 0.10, i.e., it is much larger than the optimal mismatch for growing a MC shell (0.04), and quite close to the optimal mismatch for a AM one (0.12, as estimated by geometrical considerations). On the other hand, the optimal mismatch for the formation of a Ch1 shell is quite larger (0.14, see Fig. 8a). If the growth is continued by depositing Ag atoms, shells $(2, 3)^*$ and then $(3, 3)$ form. Such AM growth pathway appears to be unaffected by the mismatch since it is observed also in the case of zero mismatches of Fig. 8b. However, as for the CK shells, one can estimate the optimal size mismatch for changing the AM class, finding values sensibly larger than zero, and in the same range of those calculated for the CK shells. Therefore, depositing atoms of larger size, such as Ag (the mismatch between Pd and Ag is 0.05), is expected to be beneficial for the stability of the resulting aggregate. Further deposition of Ag atoms leads to the formation of a chiral Ch3 shell, of type $(3, 4)$. Indeed, the $(3, 3)$ BG shell can be seen both as a generalised AM and a CK shell, and therefore it allows to obtain a very peculiar growth sequence, in which the two families of icosahedral shells are present in the same structure. We remark that the growth on top of a BG shell naturally leads to the formation of a chiral shell instead of an AM one, due to the lack of fourfold adsorption sites that are needed to form AM shells of class larger than 1.

From the energetic point of view, also the generalised anti-Mackay structures may present notable stability. In fact, $Ni_{147}@Pd_{132}$ and $Ni_{147}@Pd_{132}@Ag_{192}$ generalised anti-Mackay structures are the lowest in energy (see also Supplementary Note 4.1).

Discussion

Here, we discuss the potential applications of the icosahedral structures described in this work, and we suggest possible extensions of our design strategy.

In many cases, the applications of nanoparticles stem from the structure of their surface. Our work shows that to obtain a specific type of surface shell, it is necessary to build the correct sequence of shells in the inner part of the nanoparticles. This is possible if different elements (two or more) are used, with the appropriate mismatch.

Applications of different kinds are also possible. For metal nanoparticles, it may be useful to protect a core (for example a magnetic core made of Ni, Co or Fe) by covering it with another metal. Our results indicate that for this purpose the size mismatch must be carefully chosen, depending also on the size of the magnetic core. If not, other asymmetric quasi-Janus structures with off-centred cores would be much more stable (for example, see ref. 46 and Supplementary Fig. 15), and the core would be protected much less effectively.

In this work, we have treated specific examples related to metal clusters and nanoparticles. However, we believe that our construction can be relevant for other systems, e.g., colloidal aggregates. Colloids interact by potentials with very short range[47]. In Supplementary Note 1.6 we have shown that, for systems with short-range interaction, it is still possible to build stable structures according to our rules. However, the structures are less tolerant of deviations from the optimal size mismatch between shells, therefore being stable in a narrower range of mismatch values around the optimal one. This implies that shells must be carefully assembled to satisfy the constraints on mismatch values. In addition, we note that in some experiments on hard-sphere colloids, in which particle-particle attractive forces are negligible, icosahedral structures have been obtained in confined environments due to entropic effects[25–27]. These experiments considered colloids of equal sizes and obtained aggregates with Mackay or anti-Mackay arrangements. Our results may be relevant also for these systems, since they may give a systematic guide on how to build those confined colloidal systems using colloids with different sizes. In fact, our approach, which is mostly based on general geometric considerations, is able to indicate the appropriate size mismatch between the spheres.

A natural generalisation of the results presented here concerns in drawing paths that do not obey to the step rule $(h, k) \rightarrow (h, k + 1)$ or $(h, k) \rightarrow (h + 1, k)$. These paths are discussed in Supplementary Note 5, where we show that they are less likely to be physically relevant because they lead to poor matching between atoms in adjacent shells.

Our construction can be further generalised. Let us mention a few possibilities. First, the paths can begin at any point in the lattice,
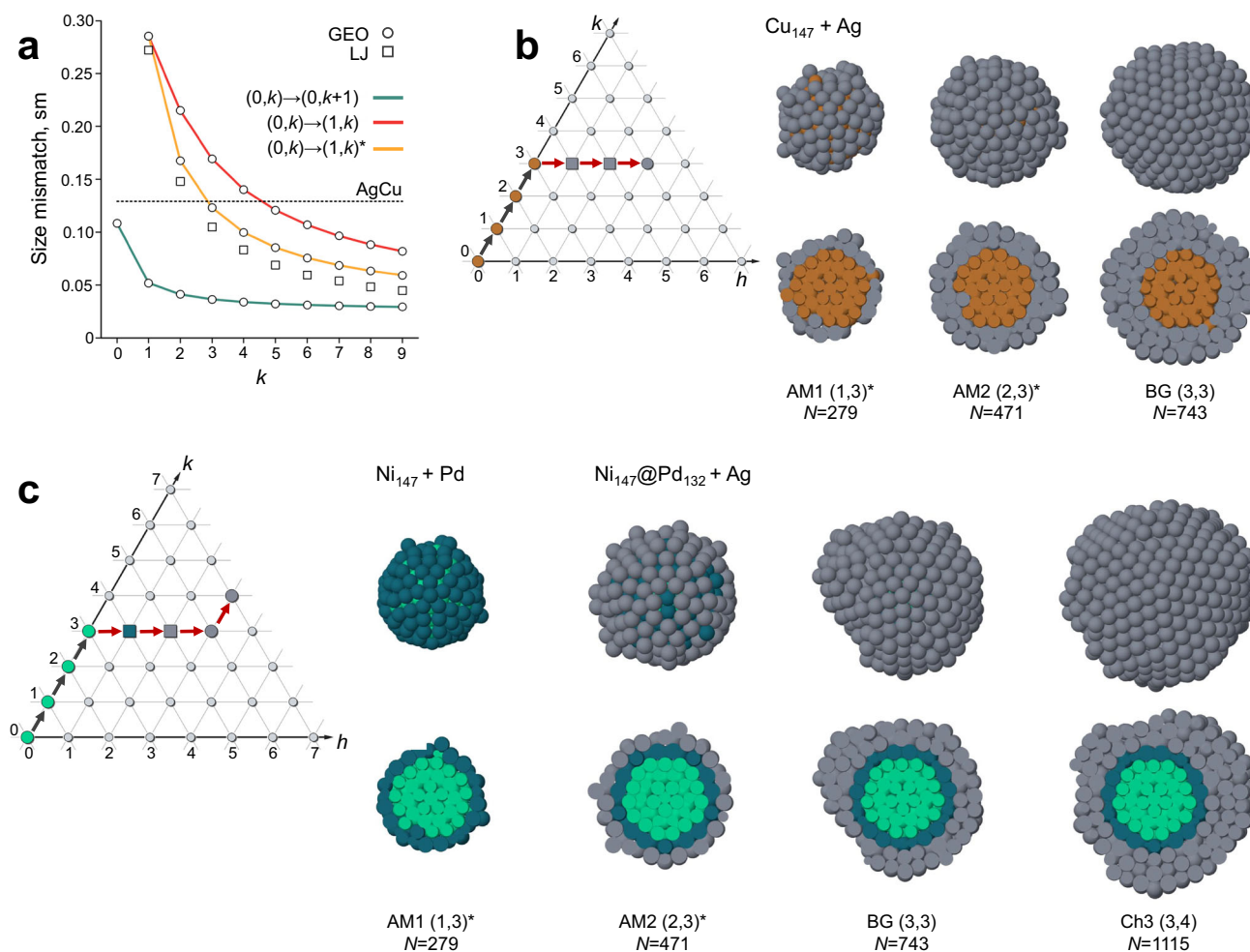
Fig. 8 | Growth of generalised anti-Mackay structures. a Optimal mismatch for one AM1 shell on a Mackay core ($(0, k) \to (1, k)^*$) as a function of core size (yellow curve), compared with Ch1 ($(0, k) \to (1, k)$) (red curve) and Mackay shells ($(0, k) \to (0, k+1)$) (blue curve), for Lennard-Jones clusters. GEO values are calculated by the formula derived in Supplementary Note 1.5. The mismatch between Ag and Cu is indicated. **b, c** Snapshots from MD growth simulations (with cluster surfaces and cross sections shown in top and bottom lines, respectively) and corresponding paths, with AM shells indicated by squares. In (**b**) Ag atoms are deposited on a Mackay Cu_{147} core. In (**c**) Pd atoms are deposited on a Ni core, and then Ag atoms are deposited on the Ni@Pd cluster. In the top and bottom rows of the snapshot sequences, we show the cluster surface and its cross-section, respectively. In the representation of shell sequences in the hexagonal plane, black arrows are used to connect the shells belonging to the initial icosahedral seed, while red arrows connect the shells spontaneously formed on top of it in the growth simulations. Ni, Cu, Pd and Ag atoms are coloured in light green, orange, blue and grey, respectively. Source data of (**a**) are provided as a Source Data file.

instead of (0,0), so that the shells enclose an empty volume. Multi-shell structures enclosing a cavity are relevant to biological systems[34,48,49] and have been observed in metal clusters[41]. Second, the non-equivalent sites of a shell can be decorated with different types of particles, while maintaining icosahedral symmetry. For example, the vertex atoms in the surface shell of a metal cluster can be of a different species than the other atoms, thus becoming isolated impurities embedded in the surface of a different material. This possibility is relevant to single-atom catalysis[50]. Moreover, the mapping into paths may be applied to other figures obtained by cutting and folding the hexagonal lattice, such as octahedra and tetrahedra, and to other lattices, including Archimedean lattices[16], that can better accommodate particles with non-spherically symmetric interactions.

In summary, the mapping into paths is a powerful tool for the bottom-up design of chiral and achiral aggregates of atoms, colloids and complex molecules. The unusual geometries of these aggregates can be of interest in various fields, e.g., in catalysis, optics and synthetic biology.

Methods

Construction of the structures

Icosahedral structures are built by assembling Caspar-Klug and anti-Mackay shells by our C++ code. The code takes as input the geometric features of each shell, i.e., the indexes h and k of the CK construction, the distance d between particles, and the shell type (either CK or AM). For CK shells, the first 12 particles are placed in the vertices of the icosahedron of edge legth $\sin(2\pi/5)\sqrt{T}\,d$. The other particles are placed on the icosahedral facets according to the CK scheme: on each facet plane, a 2D hexagonal lattice is built, which is rotated at an angle of amplitude θ_{CK} with respect to one of the facet edges; particles are placed on lattice points falling within the facet. For AM shells, the indexes p and q are calculated as $p = k - h + 1$, $q = h - 1$ if $k \geq h$, $p = h - k + 1$, $q = k - 1$ otherwise. The first 12 particles are placed in the vertices of the icosahedron of edge length $(p + \sqrt{3}\,q + \sqrt{3} - 1)\,d$. The other particles are placed on the icosahedral facets according to the scheme of Fig. 6a. A more detailed description of CK and AM shells and of the procedure for constructing them can be found in Supplementary Note 1.

LJ and Morse potential calculations

Both potentials are pair potentials, in which the total energy E is written as

$$E = \frac{1}{2} \sum_{i \neq j} u(r_{ij}), \tag{5}$$

where $r_{ij} = |\mathbf{r}_j - \mathbf{r}_i|$ is the distance between a pair of particles. The LJ potential is written as

$$u(r) = \varepsilon \left[\left(\frac{r_m}{r} \right)^{12} - 2 \left(\frac{r_m}{r} \right)^6 \right], \tag{6}$$

where ε is the well depth and r_m is the equilibrium distance, which corresponds to the particle size d. The Morse potential is written as

$$u(r) = \varepsilon \left[e^{-2\alpha(r/r_m - 1)} - 2e^{-\alpha(r/r_m - 1)} \right], \tag{7}$$

where the dimensionless parameter α regulates the width of the potential well, that decreases with increasing α. For $\alpha = 6$ both LJ and Morse potential have the same width of the well, i.e., the same curvature at the well bottom. For $\alpha < 6$ the potential well is wider than in LJ. The chosen values $\alpha = 4, 5$ give widths of the potential well similar to those for the interaction between metal atoms. In the simulations of Figs. 3a–d and 8a all particles were given the same value of ε (and of α for the Morse potential), but particles of the outer shell and of the core were given different sizes (i.e., $r_m = r_{m,c}$ for core particles and $r_m = r_{m,s}$ for outer shell particles). For interactions between particles of the core and the outer shell $r_{m,cs} = (r_{m,c} + r_{m,s})/2$. The structures were locally relaxed by quenched molecular dynamics[51] to reach the position of the local minimum in the energy landscape.

Global optimisation searches

Global optimisation searches are performed by the Basin Hopping algorithm[52] and its extensions[53,54]. In all cases, at least four independent unseeded simulations of 1-4 $\times 10^6$ steps were performed, plus some seeded simulations starting from selected structures. All global minima reported here and in Supplementary Note 4.1 resulted from unseeded simulations. For all systems, atom-atom interactions were modelled by an atomistic force field, which is known as Gupta potential[55]. Form and parameters of the potential can be found in refs. 56–59.

DFT calculations

All DFT calculations were made by the open-source QUANTUM ESPRESSO software[60] using the Perdew-Burke-Ernzerhof exchange-correlation functional[61]. The convergence thresholds for the total energy, total force, and electronic calculations were set to 10^{-4} Ry, 10^{-3} Ry at.u^{-1}. and 5×10^{-6} Ry respectively. We used a periodic cubic cell, whose size was set to 26-48 Å, depending on the size of the cluster, in order to ensure at least a 10 Å separation between clusters in different periodic images. Cutoffs for wavefunction and charge density were set to 66 and 323 Ry, according to Na.pbe-spn-kjpaw_psl.1.0.0.UPF, K.pbe-spn-kjpaw_psl.1.0.0.UPF, Rb.pbe-spn-kjpaw_psl.1.0.0.UPF as provided by the QUANTUM ESPRESSO pseudopotential library available at http://pseudopotentials.quantum-espresso.org/legacy_tables/ps-library/.

MD growth simulations

Molecular dynamics growth simulations are made by molecular dynamics using the same type of procedure adopted in refs. 24,44. The equations of motion are solved by the Velocity Verlet algorithm with a time step of 5 fs for the simulations of AgNi, AgCu, AgCo, AuCo, AuFe, AgPdNi and 2 fs for the simulations of NaK, NaRb, NaKRb, NaRbCs. In all simulations, the temperature is kept constant by an Andersen thermostat with a collision frequency of 5×10^{11} s^{-1}. Simulations start from a seed, which is an initial cluster, and then atoms are deposited one by one on top of it in an isotropic way from random directions at a constant rate. The simulation of Fig. 6a was started from a Na$_{13}$@K$_{32}$ Bergman-type seed corresponding to the path arriving to $(h, k) = (1, 1)$ and Rb atoms were deposited at a rate of 0.1 atoms ns^{-1} and at a temperature of 125 K. The simulation of Fig. 6b was started from a Na$_{13}$@Rb$_{32}$@Rb$_{72}$ chiral seed corresponding to the path arriving to $(h, k) = (1, 2)$ and Cs atoms were deposited at a rate of 0.1 atoms ns^{-1} at 125 K. The simulation of Fig. 6c was started from a Ni$_{147}$ Mackay icosahedral seed corresponding to the path arriving at $(h, k) = (0, 3)$ and Ag atoms were deposited at a rate of 0.1 atoms ns^{-1} at 450 K. The simulation of Fig. 6d was started from a Cu$_{561}$ Mackay icosahedral seed corresponding to the path arriving at $(h, k) = (0, 5)$ and Ag atoms were deposited at a rate of 0.1 atoms ns^{-1} at 450 K. The simulation of Fig. 8b was started from a Cu$_{147}$ Mackay icosahedral seed corresponding to the path arriving at $(h, k) = (0, 3)$ and Ag atoms were deposited at a rate of 1 atom ns^{-1} at 350 K. The simulations of Fig. 8c were started from a Ni$_{147}$ Mackay icosahedral seed corresponding to the path arriving at $(h, k) = (0, 3)$ and Pd atoms were deposited at a rate of 0.1 atoms ns^{-1} at 400 K. Then Ag atoms were deposited on a Ni$_{147}$@Pd$_{132}$ seed terminated by a $(1, 3)^*$ AM1 shell, at a rate of 0.1 atoms ns^{-1} at 300 K. For all systems, atom-atom interactions were modelled by an atomistic force field, which is known as Gupta potential[55]. The form and parameters of the potential can be found in refs. 56–59.

Reporting summary

Further information on research design is available in the Nature Portfolio Reporting Summary linked to this article.

Data availability

The data that support the findings of this study are available from the corresponding authors upon request. Source data are provided in this paper.

Code availability

Codes used in this study, such as for the MD simulations and for constructing the multi-shell icosahedra, are available from the corresponding authors upon request.

References

1. Yao, Y. et al. High-entropy nanoparticles: Synthesis-structure-property relationships and data-driven discovery. *Science* **376**, eabn3103 (2022).
2. Yao, Y. et al. Computationally aided, entropy-driven synthesis of highly efficient and durable multi-elemental alloy catalysts. *Sci. Adv.* **6**, eaaz0510 (2020).
3. Xie, P. et al. Highly efficient decomposition of ammonia using high-entropy alloy catalysts. *Nat. Commun.* **10**, 4011 (2019).
4. Yan, J. et al. Anomalous size effect on yield strength enabled by compositional heterogeneity in high-entropy alloy nanoparticles. *Nat. Commun.* **13**, 2789 (2022).
5. Howes, P. D., Chandrawati, R. & Stevens, M. M. Colloidal nano-particles as advanced biological sensors. *Science* **346**, 1247390 (2014).
6. Chen, L. et al. Imparting multi-functionality to covalent organic framework nanoparticles by the dual-ligand assistant encapsulation strategy. *Nat. Commun.* **12**, 4556 (2021).
7. Wang, D. et al. Structurally ordered intermetallic platinum-cobalt core-shell nanoparticles with enhanced activity and stability as oxygen reduction electrocatalysts. *Nat. Mater.* **12**, 81 (2013).
8. Huo, Q. et al. A new class of silica cross-linked micellar core-shell nanoparticles. *J. Am. Chem. Soc.* **128**, 6447–6453 (2006).
9. Vega-Paredes, M. et al. Electrochemical stability of rhodium-platinum core-shell nanoparticles: An identical location scanning

transmission electron microscopy study. *ACS Nano* **17**, 16943–16951 (2023).

10. Foucher, A. C. et al. Structure and stability of core-shell Cu-Pt nanoparticles for catalytic applications. *Chem. Mater.* **35**, 8758–8764 (2023).

11. Nelli, D., Roncaglia, C. & Minnai, C. Strain engineering in alloy nanoparticles. *Adv. Phys. X* **8**, 2127330 (2023).

12. Strasser, P. et al. Lattice-strain control of the activity in dealloyed core-shell fuel cell catalysts. *Nat. Chem.* **2**, 454–460 (2010).

13. Mackay, A. L. A dense non-crystallographic packing of equal spheres. *Acta Crystallogr.* **15**, 916–918 (1962).

14. Caspar, D. L. D. & Klug, A. Physical principles in the construction of regular viruses. *Cold Spring Harb. Symp. Quant. Biol.* **27**, 1–24 (1962).

15. Sadre-Marandi, F. & Das, P. Extension of Caspar-Klug theory to higher order pentagonal polyhedra. *Computational Mathematical Biophysics* **6**, 1–13 (2018).

16. Twarock, R. & Luque, A. Structural puzzles in virology solved with an overarching icosahedral design principle. *Nat. Commun.* **10**, 4414 (2019).

17. Martin, T. P. Shells of atoms. *Phys. Rep.* **273**, 199–241 (1996).

18. Baletto, F. & Ferrando, R. Structural properties of nanoclusters: Energetic, thermodynamic, and kinetic effects. *Rev. Mod. Phys.* **77**, 371–423 (2005).

19. Li, S., Roy, P., Travesset, A. & Zandi, R. Why large icosahedral viruses need scaffolding proteins. *Proc. Natl. Acad. Sci.* **115**, 10971–10976 (2018).

20. Farges, J., de Feraudy, M., Raoult, B. & Torchet, G. Structure and temperature of rare gas clusters in a supersonic expansion. *Surf. Sci.* **106**, 95–100 (1981).

21. Wang, Z. W. & Palmer, R. E. Determination of the ground-state atomic structures of size-selected au nanoclusters by electron-beam-induced transformation. *Phys. Rev. Lett.* **108**, 245502 (2012).

22. Langille, M. R., Zhang, J., Personick, M. L., Li, S. & Mirkin, C. A. Stepwise evolution of spherical seeds into 20-fold twinned icosahedra. *Science* **337**, 954–957 (2012).

23. Hubert, H. et al. Icosahedral packing of B_{12} icosahedra in boron suboxide (B_6O). *Nature* **391**, 376–378 (1998).

24. Nelli, D. et al. Sudden collective atomic rearrangements trigger the growth of defect-free silver icosahedra. *Nanoscale* **15**, 18891–18900 (2023).

25. de Nijs, B. et al. Entropy-driven formation of large icosahedral colloidal clusters by spherical confinement. *Nat. Mater.* **14**, 56–60 (2015).

26. Wang, J. et al. Magic number colloidal clusters as minimum free energy structures. *Nat. Commun.* **9**, 5259 (2018).

27. Chen, Y. et al. Morphology selection kinetics of crystallization in a sphere. *Nat. Phys.* **17**, 121–127 (2021).

28. Shechtman, D., Blech, I., Gratias, D. & Cahn, J. W. Metallic phase with long-range orientational order and no translational symmetry. *Phys. Rev. Lett.* **53**, 1951–1953 (1984).

29. Noya, E. G., Wong, C. K., Llombart, P. & Doye, J. P. K. How to design an icosahedral quasicrystal through directional bonding. *Nature* **596**, 367–371 (2021).

30. Pankova, A. A., Akhmetshina, T. G., Blatov, V. A. & Proserpio, D. M. A collection of topological types of nanoclusters and its application to icosahedron-based intermetallics. *Inorg. Chem.* **54**, 6616–6630 (2015).

31. Rossmann, M. G. & Johnson, J. E. Icosahedral RNA virus structure. *Annu. Rev. Biochem.* **58**, 533–569 (1989).

32. Salunke, D., Caspar, D. & Garcea, R. Polymorphism in the assembly of polyomavirus capsid protein VP1. *Biophys. J.* **57**, 887–900 (1989).

33. Yeates, T. O., Thompson, M. C. & Bobik, T. A. The protein shells of bacterial microcompartment organelles. *Curr. Opin. Struct. Biol.* **21**, 223–231 (2011).

34. Zandi, R., Dragnea, B., Travesset, A. & Podgornik, R. On virus growth and form. *Phys. Rep.* **847**, 1–102 (2020).

35. Douglas, S. M. et al. Self-assembly of DNA into nanoscale three-dimensional shapes. *Nature* **459**, 414–418 (2009).

36. Martín-Bravo, M., Llorente, J. M. G., Hernández-Rojas, J. & Wales, D. J. Minimal design principles for icosahedral virus capsids. *ACS Nano* **15**, 14873–14884 (2021).

37. Pinto, D. E. P., Šulc, P., Sciortino, F. & Russo, J. Design strategies for the self-assembly of polyhedral shells. *Proc. Natl. Acad. Sci. USA* **120**, e2219458120 (2023).

38. Bergman, G., Waugh, J. L. & Pauling, L. The crystal structure of the metallic phase $Mg_{32}(A1, Zn)_{49}$. *Acta Cryst.* **10**, 254 (1957).

39. Bochicchio, D. & Ferrando, R. Size-dependent transition to high-symmetry chiral structures in AgCu, AgCo, AgNi, and AuNi nanoalloys. *Nano Lett.* **10**, 4211–4216 (2010).

40. Settem, M. & Kanjarla, A. K. On the nature of the structural transitions between anti-mackay stacking, chiral stacking and their thermal stability in AgCu nanoalloys. *Comput. Mater. Sci.* **184**, 109822 (2020).

41. Whetten, R. L. et al. Chiral-icosahedral (*I*) symmetry in ubiquitous metallic cluster compounds (145A,60X): Structure and bonding principles. *Acc. Chem. Res.* **52**, 34–43 (2019).

42. Branz, W., Malinowski, N., Enders, A. & Martin, T. P. Structural transition in (C60)$_n$ clusters. *Phys. Rev. B* **66**, 094107 (2002).

43. Koga, K. & Sugawara, K. Population statistics of gold nanoparticle morphologies: direct determination by HREM observations. *Surf. Sci.* **529**, 23–35 (2003).

44. Xia, Y., Nelli, D., Ferrando, R., Yuan, J. & Li, Z. Y. Shape control of size-selected naked platinum nanocrystals. *Nat. Commun.* **12**, 3019 (2021).

45. Wang, J. et al. Free energy landscape of colloidal clusters in spherical confinement. *ACS Nano* **13**, 9005–9015 (2019).

46. Bochicchio, D. & Ferrando, R. Morphological instability of core-shell metallic nanoparticles. *Phys. Rev. B* **87**, 165435 (2013).

47. Cerbelaud, M. et al. Numerical study of the effect of particle size dispersion on order within colloidal assemblies. *Mater. Today Commun.* **38**, 107973 (2024).

48. Prinsen, P., van der Schoot, P., Gelbart, W. M. & Knobler, C. M. Multishell structures of virus coat proteins. *J. Phys. Chem. B* **114**, 5522–5533 (2010).

49. Sasaki, E. & Hilvert, D. Self-assembly of proteinaceous multishell structures mediated by a supercharged protein. *J. Phys. Chem. B* **120**, 6089–6095 (2016).

50. Wang, A., Li, J. & Zhang, T. Heterogeneous single-atom catalysis. *Nat. Rev. Chem.* **2**, 65–81 (2018).

51. Bennett, C. H. in *Diffusion in Solids: Recent Developments*, Edited by A. S. Nowick and J. J. Burton. (Academic Press, New York, 1975).

52. Wales, D. J. & Doye, J. P. K. Global optimization by basin-hopping and the lowest energy structures of Lennard-Jones clusters containing up to 110 atoms. *J. Phys. Chem. A* **101**, 5111–5116 (1997).

53. Rossi, G. & Ferrando, R. Searching for low-energy structures of nanoparticles: a comparison of different methods and algorithms. *J. Phys. Cond. Mat.* **21**, 084208 (2009).

54. Rapetti, D., Roncaglia, C. & Ferrando, R. Optimizing the shape and chemical ordering of nanoalloys with specialized walkers. *Adv. Theory Simul.* **6**, 2300268 (2023).

55. Gupta, R. P. Lattice relaxation at a metal surface. *Phys. Rev. B* **23**, 6265 (1981).

56. Li, Y., Blaisten-Barojas, E. & Papaconstantopoulos, D. A. Structure and dynamics of alkali-metal clusters and fission of highly charged clusters. *Phys. Rev. B* **57**, 15519–15532 (1998).

57. Baletto, F., Mottet, C. & Ferrando, R. Growth simulations of silver shells on copper and palladium nanoclusters. *Phys. Rev. B* **66**, 155420 (2002).

58. Baletto, F., Mottet, C. & Ferrando, R. Growth of three-shell onionlike bimetallic nanoparticles. *Phys. Rev. Lett.* **90**, 135504 (2003).
59. Rossi, G., Schiappelli, G. & Ferrando, R. Formation pathways and energetic stability of icosahedral $Ag_{shell}Co_{core}$ nanoclusters. *J. Comput. Theor. Nanosci.* **6**, 841 (2009).
60. Giannozzi, P. et al. Quantum espresso: a modular and open-source software project for quantum simulations of materials. *J. Phys. Condens. Matter* **21**, 395502 (2009).
61. Perdew, J. P., Burke, K. & Ernzerhof, M. Generalized gradient approximation made simple. *Phys. Rev. Lett.* **77**, 3865–3868 (1996).

Acknowledgements

Author contributions

N.C. performed and analysed the growth simulations. D.N. developed the analytical calculations of mismatch, made the DFT calculations and developed the code for constructing chiral and anti-Mackay shells. R.F. made Lennard-Jones and Morse calculations. D.N. and R.F. made the global optimisation searches and supervised the work. All authors contributed to writing the paper.

Competing interests

The authors declare no competing interests.

Additional information

Supplementary information The online version contains supplementary material available at https://doi.org/10.1038/s41467-025-56952-1.

Correspondence and requests for materials should be addressed to Diana Nelli or Riccardo Ferrando.

Peer review information *Nature Communications* thanks Szilard Fejer and the other anonymous reviewer(s) for their contribution to the peer review of this work. A peer review file is available.

Reprints and permissions information is available at http://www.nature.com/reprints

Publisher's note Springer Nature remains neutral with regard to jurisdictional claims in published maps and institutional affiliations.